Monthly Notices
of the
ROYAL ASTRONOMICAL SOCIETY

MNRAS **481,** 5046–5061 (2018)
Advance Access publication 2018 September 10

doi:10.1093/mnras/sty2484

Prospects for gamma-ray observations of narrow-line Seyfert 1 galaxies with the Cherenkov Telescope Array

P. Romano [1]★ S. Vercellone [1] L. Foschini [1] F. Tavecchio,[1] M. Landoni[1] and J. Knödlseder[2]

[1]*INAF, Osservatorio Astronomico di Brera, Via E. Bianchi 46, I-23807 Merate, Italy*
[2]*Institut de Recherche en Astrophysique et Planétologie, 9 avenue Colonel-Roche, F-31028 Toulouse Cedex 4, France*

Accepted 2018 September 6. Received 2018 August 27; in original form 2018 July 25

ABSTRACT

Gamma-ray-emitting narrow-line Seyfert 1 (γ-NLS1) galaxies are thought to harbour relatively low-mass black holes (10^6–10^8 $M_\odot$) accreting close to the Eddington limit. They show characteristics similar to those of blazars, such as flux and spectral variability in the gamma-ray energy band and radio properties which point towards the presence of a relativistic jet. These characteristics make them an intriguing class of sources to be investigated with the Cherenkov Telescope Array (CTA), the next-generation ground-based gamma-ray observatory. We present our extensive set of simulations of all currently known γ-ray emitters identified as NLS1s (20 sources), investigating their detections and spectral properties, taking into account the effect of both the extragalactic background light in the propagation of gamma-rays and intrinsic absorption components. We find that the prospects for observations of γ-NLS1 with CTA are promising. In particular, the brightest sources of our sample, SBS 0846+513, PMN J0948+0022, and PKS 1502+036, can be detected during high/flaring states, the former two even in the case in which the emission occurs within the highly opaque central regions, which prevent gamma-rays above a few tens of GeV to escape. In this case, the low-energy threshold of CTA will play a key role. If, on the other hand, high-energy emission occurs outside the broad-line region, we can detect the sources up to several hundreds of GeV – depending on the intrinsic shape of the emitted spectrum. Therefore, CTA observations will provide valuable information on the physical conditions and emission properties of their jets.

Key words: galaxies: jets – galaxies: Seyfert – gamma rays: galaxies.

1 INTRODUCTION

Narrow-line Seyfert 1 (NLS1) galaxies are a subclass of active galactic nuclei (AGNs) characterized in the optical regime by narrow permitted emission lines [Hβ full width at half-maximum (FWHM) $< 2000\,\mathrm{km\,s^{-1}}$; Goodrich 1989], weak forbidden [O III] lines ([O III] λ5007/Hβ < 3), and strong iron emission lines (high Fe II/Hβ; Osterbrock & Pogge 1985). As such, these galaxies are located at the lower end of the line-width distribution for the Seyfert 1 population, thus distinguished from the bulk of Seyfert 1 galaxies (broad-line Seyfert 1s, BLS1s). In the X-rays, NLS1s have equally extreme properties, as they show rapid and large amplitude variability (Boller, Brandt & Fink 1996), with some showing X-ray flares up to a factor of 100 in flux, on time-scales of days, compared to the factors of a few seen in BLS1s. These distinctive properties can be understood in terms of lower masses of the central black hole (10^6–10^8 $M_\odot$) compared to BLS1s with similar luminosities and higher accretion rates, close to the Eddington limit (e.g. Peterson et al. 2004).

Traditionally, NLS1s are considered to be hosted in spiral/barred galaxies (Crenshaw, Kraemer & Gabel 2003), and generally not strong radio emitters, but evidence has been collected that a small fraction (4–7 per cent; Komossa et al. 2006; Cracco et al. 2016) of NLS1s are radio loud and show a flat radio spectrum (Oshlack, Webster & Whiting 2001; Zhou et al. 2003; Yuan et al. 2008; see also Lähteenmäki et al. 2017). Furthermore, a hard component was found in the *Swift*/XRT X-ray spectra of NLS1s, as well as spectral variability in the hard X-ray as observed by INTEGRAL/IBIS and *Swift*/BAT (Foschini et al. 2009). These properties are strongly reminiscent of those of jetted sources (see e.g. Foschini 2012; Foschini et al. 2015; D'Ammando et al. 2016a).

The first detection by *Fermi*-LAT of an NLS1 in the gamma-rays ($E > 100$ MeV), PMN J0948+0022 (Abdo et al. 2009a; Foschini et al. 2010), and subsequent follow-ups (Abdo et al. 2009b; Foschini et al. 2011b) confirmed that its multiwavelength behaviour was that

★ E-mail: patrizia.romano@inaf.it

of a source with a relativistic jet, like those observed in blazars. Since then, a total of 20 sources identified as NLS1s have been found by *Fermi*-LAT to emit in the gamma-rays and the sample is bound to grow in time. However, currently no firm detection has been obtained in the very high-energy (VHE) regime. Indeed, Falcone et al. (2004) found marginal evidence for flaring (at the 2.5σ level) but did not detect significant emission from 1H 0323+342 with *Whipple* above 400 GeV. Also, VERITAS observations of PMN J0948+0022 (5 h) only yielded upper limits at E >100 GeV (D'Ammando et al. 2015a). A third NLS1, PKS 2004−447, was observed but not detected at VHE by H.E.S.S. (H. E. S. S. Collaboration 2014). Detection in the VHE regime would provide important clues on the location of the emitting region, since the central region of NLS1s, analogously to that of flat-spectrum radio quasars (FSRQ), is expected to be highly opaque to gamma-rays above a few tens of GeV.

The future of NLS1 science in the VHE regime will benefit from the construction of the Cherenkov Telescope Array (CTA; Actis et al. 2011; Acharya et al. 2013), which will afford us a wide (20 GeV–300 TeV) energy range. The CTA array will include different classes of telescopes, i.e. the large-sized telescopes (LSTs, diameter D $\sim$ 23 m), the medium-sized telescopes (MSTs, D $\sim$ 12 m), and the small-sized telescopes (SSTs, primary mirror D $\sim$ 4 m). The full array will be installed at two sites, one for each hemisphere to allow an all-sky coverage. The baseline CTA set-up (Hofmann 2017b,a) is composed of a northern site, located at the Observatorio del Roque de los Muchachos on the island of La Palma (Spain), where 4 LSTs and 15 MSTs, covering an area of $\sim$1 km^2, will be installed, and a southern site, located at the European Southern Observatory's (ESO's) Paranal Observatory in the Atacama Desert (Chile), which will cover an area of about 4 km^2, where 4 LSTs, 25 MSTs, and 70 SSTs will be installed. CTA will provide an average differential sensitivity a factor of 5–20 times better with respect to the current imaging atmospheric Cherenkov telescope (IACT) arrays; in particular for transients and flaring events (time-scales of $\sim$1 d or shorter) CTA will be about two orders of magnitude more sensitive with respect to *Fermi*-LAT at the overlapping energy of 25 GeV, thus allowing an unprecedented opportunity to investigate flaring gamma-ray-emitting narrow-line Seyfert 1 (γ-NLS1) galaxies.

In this paper, we consider all currently known γ-NLS1s and explore the prospects for observations of the whole sample with CTA. In Section 2, we define our sample of NLS1s, in Section 3, we describe our simulation set-up, in Section 4 we present our results, and in Section 5we discuss their implications.

2 DATA SAMPLE

Our sample (Table 1) consists of all objects classified as NLS1s that have been detected in the gamma-rays, as mainly reported by the *Fermi*-LAT 8-year Source List (FL8Y, `gll_psc_8year_v3.fit` v. 2018-01-03)[1] and in the existing literature. Although the sample is not complete in the statistical sense, since it is not characterized by a flux limit, it does include all γ-NLS1s (as well as two candidates; see the footnotes of Table 1) identified at the time of writing.

Table 1 includes, for each source, coordinates (Equatorial, J2000, column 3, 4) and redshift (column 5) as provided by the NASA/IPAC Extragalactic Database (NED).[2] It also reports the spectral parameters for the best-fitting models to the *Fermi* data that we adopted for each source (and flux state, columns 6–10), and the reference from which it was drawn or derived (column 11). The spectral models are

(i) a power law (PL),

$$\frac{\mathrm{d}N}{\mathrm{d}E} = K_0 \left(\frac{E}{E_0}\right)^{-\Gamma}, \quad (1)$$

where K_0 is the normalization (in units of ph cm^{-2} s^{-1} MeV^{-1}), E_0 is the pivot energy (in MeV), and Γ is the power-law photon index;

(ii) a log-parabola (LP)

$$\frac{\mathrm{d}N}{\mathrm{d}E} = K_0 \left(\frac{E}{E_0}\right)^{-\alpha-\beta\ln(E/E_0)}, \quad (2)$$

where K_0 is the normalization, E_0 is the pivot energy, α is the spectral slope, and β is the curvature;

(iii) a broken power law (BKPL)

$$\frac{\mathrm{d}N}{\mathrm{d}E} = K_0 \times \begin{cases} \left(\frac{E}{E_\mathrm{b}}\right)^{-\Gamma_1} & \text{if } E < E_\mathrm{b} \\ \left(\frac{E}{E_\mathrm{b}}\right)^{-\Gamma_2} & \text{otherwise,} \end{cases} \quad (3)$$

where K_0 is the normalization and Γ_1 and Γ_2 are the spectral indices at energies lower and higher than the break energy E_b.

3 SIMULATIONS

The simulations were performed with the `ctools` (Knödlseder et al. 2016, v. 1.4.2)[3] analysis package and the public CTA instrument response files[4] (IRF, v. prod3b-v1). Each source is assumed to be observed from the site that provides the largest source elevation, computed from the difference between the geographic latitudes of the CTA sites (north latitude: 28.76 N; south latitude: 24.68 S) and the source declination (Table 1, column 4); accordingly, the corresponding prod3b-v1 IRFs (reported in Table 2, column 3) were used for the simulations.

In the model definition XML file for `ctools`, the spectral model component was defined as a `FileFunction` type so that the spectrum was provided as an ASCII file containing energy (in MeV) and differential flux values (in units of ph cm^{-2} s^{-1} MeV^{-1}), described according to

$$M_\mathrm{spectral}(E) = N_0 \frac{\mathrm{d}N}{\mathrm{d}E}, \quad (4)$$

where N_0 is the normalization.

The input spectral models have been derived by extrapolating the best-fitting *Fermi* spectra (the parameters are reported in Table 1) to the CTA energy range, including the effects of the gamma-ray absorption both along the path to the Earth (which, at the relevant energies, is due to the interaction with the ultraviolet (UV)-optical part of the extragalactic background light, EBL), and inside the source (internal absorption). The correction for absorption by the EBL (providing substantial attenuation only above about 100 GeV) has been applied to all spectra by using the model of Domínguez et al. (2011).

Absorption of gamma-rays within the source itself is expected because of the interaction with the UV ambient radiation (originating in the accretion disc and in the broad-line region, BLR; see e.g. Poutanen & Stern 2010). Because of the presence of the prominent

[1] https://fermi.gsfc.nasa.gov/ssc/data/access/lat/fl8y/.
[2] https://ned.ipac.caltech.edu.
[3] http://cta.irap.omp.eu/ctools/.
[4] https://www.cta-observatory.org/science/cta-performance/.

Table 1. Sample of γ-NLS1 and spectral parameters adopted for the simulations.

Source name	Common name	RA	Dec.	z	Model					Ref.
					PL	K_0	E_0	Γ		
					LP			α	β	
					BKPL		E_b	Γ_1	Γ_2	
		(deg)	(deg)			(ph cm^{-2} MeV^{-1} s^{-1})	(MeV)			
FL8Y J0324.7+3411	1H 0323+342	51.19	34.20	0.061	PL	2.00×10^{-11}	436	2.93	–	1
FL8Y J0850.0+5108	SBS 0846+513	132.51	51.14	0.585	LP	7.83×10^{-12}	638	2.12	0.10	1
High state	–	–	–	–	PL	1.08×10^{-10}	300	2.10	–	2
FL8Y J0932+5306	NVSS J093241+530633	143.17	53.11	0.597	PL	1.10×10^{-11}	300	2.39	–	3
3FGL J0937.7+5008[a, b]	GB6 J0937+5008	144.30	50.15	0.276	PL	8.00×10^{-12}	300	2.41	–	3
FL8Y J0948.9+0022	PMN J0948+0022	147.24	0.37	0.585	BKPL	1.06×10^{-10}	1000	2.30	3.40	4
High state	–	–	–	–	PL	9.60×10^{-10}	300	2.55	–	5
'Flare' state	–	–	–	–	PL	2.88×10^{-9}	300	2.55	–	6
FL8Y J0958.0+322[c]	CRATES J095821+32235	149.52	32.37	0.530	PL	1.76×10^{-12}	538	2.73	–	1
J1102+2239	–	165.70	22.63	0.453	PL	1.40×10^{-10}	300	3.10	–	7
J1222+0413	–	185.64	4.21	0.966	PL	2.01×10^{-11}	444	2.87	–	1[d]
J1246+0238	–	191.83	2.53	0.363	PL	1.18×10^{-10}	300	3.10	–	7
FL8Y J1305.2+5108	SDSS J130522.74+511640.2[e]	196.31	51.14	0.785	PL	1.57×10^{-12}	437	2.91	–	1
FL8Y J1331.0+3031	3C 286[f]	202.75	30.53	0.850	PL	9.37×10^{-14}	1445	2.37	–	1
NVSS J142106+385522[g]	–	215.28	38.92	0.489	PL	4.00×10^{-12}	300	2.66	–	3
FL8Y J1443.1+4729	B3 1441+476[e]	220.80	47.49	0.706	PL	1.08×10^{-12}	614	2.65	–	1
FL8Y J1505.0+0326	PKS 1502+036	226.26	3.44	0.408	PL	1.11×10^{-11}	506	2.67	–	1
High state	–	–	–	–	PL	1.4×10^{-9}	250	2.54	–	8
3FGLJ1520.3+4209[a]	TXS 1518+423	230.17	42.19	0.484	PL	7.50×10^{-12}	300	2.67	–	3
SDSSJ164100.10+345452.7	–	250.25	34.91	0.164	PL	1.2×10^{-11}	300	2.5	–	9
FL8Y J1644+2618	FBQS J1644.9+2619	251.24	26.31	0.145	PL	2.02×10^{-12}	549	2.74	–	1
High state	–	–	–	–	PL	5.00×10^{-11}	300	2.50	–	10
Flare state	–	–	–	–	PL	6.35×10^{-10}	300	2.50	–	10
FL8YJ2007.9−4432	PKS 2004−447	301.98	−44.55	0.240	PL	4.72×10^{-12}	578	2.65	–	1
3FGL J2118.4+0013[a]	PMN J2118+0013	319.57	0.22	0.463	PL	3.20×10^{-12}	300	2.23	–	3
FL8Y J2119.2−0728	AT20G J211853−073227	319.81	−7.48	0.260	PL	3.46×10^{-12}	452	2.81	–	1

Redshifts are drawn from NED. Gamma-ray spectral models: PL = power law, LP = log-parabola, BKPL = broken power law.

[a] Previously misclassified as FSRQs (Paliya et al. 2018).

[b] Classified as a candidate NLS1 by Paliya et al. (2018), due to its relatively weak Fe II emission (Fe II/H β= 0.05).

[c] Assumed associated with NVSS J095820+322401 (Paliya et al. 2018).

[d] Also see Yao et al. (2015).

[e] Also see Liao et al. (2015).

[f] Also see Berton et al. (2017).

[g] Classified as a candidate NLS1 by Paliya et al. (2018), due to the incompleteness in its H β emission-line profile, leading to the ambiguity in the FWHM measurement.

References. For the models we adopted (1) *Fermi*-LAT 8-year Source List (FL8Y); (2) Paliya et al. (2016); (3) Paliya et al. (2018); (4) Abdo et al. (2009a); (5) Foschini et al. (2011b); (6) this work: flaring state, assumed a factor of 3 brighter than the high state; (7) Foschini (2011); (8) D'Ammando et al. (2016b); (9) Lähteenmäki et al. (2018); (10) D'Ammando et al. (2015b).

Ly α line of hydrogen, the most relevant spectral feature induced by internal absorption is a marked drop at ≈20–30 GeV. Due to the lack of a detailed physical and geometrical modelling of each source (and each state), in particular because of the currently unconstrained location of the gamma-ray-emitting region, for this paper we chose to mimic the drop with a simple analytical description, a cut-off at 30 GeV ($\propto e^{-E/E_{\rm cut}}$, $E_{\rm cut}$ = 30 GeV), while in future planned works we shall investigate the effects of more realistic BLR absorption models. There is indeed evidence of photons being detected at energies in excess of 10 GeV by *Fermi* from some of our sources, e.g. J0324+3410 (up to 32.7 GeV; Paliya, Stalin & Ravikumar 2015), SBS 0846+513 (16.5 GeV; Sahakyan, Baghmanyan & Zargaryan 2018), PKS 1502+036 (21.1 GeV; D'Ammando et al. 2016b). We applied such cut-off to all sources characterized by an unbroken power law in the LAT band. The cut-off was not considered for the cases in which the LAT spectrum is reproduced by a log-parabola, already characterized by an intrinsic curvature leading to the progressive softening of the spectrum (see Table 1 and notes on individual objects below).[5]

We considered only the instrumental background included in the IRFs (`CTAIrfBackground`) and no further contaminating astrophysical sources in the 5 deg field of view (FOV) we adopted for event extraction.

By default, energy dispersion is not considered in the `ctools` fits, but because of the spectral softness of NLS1s, our investigation of their detectability was also carried out at energies well below 100 GeV, where the effects of the energy dispersion can become important (Maier et al. 2017). Inclusion of the energy migration matrix in our simulations (`edisp=yes`) especially when performing likelihood analysis, involves computation times up to 10 times longer

[5] We note that we shall also consider a more optimistic scenario, i.e. no internal absorption, for SBS 0846+513.

Table 2. Set-up of the (`ctools`) simulations: site, IRF, exposure time, number of realizations run (N) for the detection in the full band (20–150 GeV), and number M of additional bins over which detection was performed (N_2 realizations), their exposure and energy ranges (see Section 3.1).

Source Name (Model)	Site[a]	IRF	Exp. (h)	Sim. N	Energy (GeV)	Bins M	Exp. (h)	Sim. N_2	Energy Bands (GeV)
J0324+3410	N	North_z20_average_50h	50	100	20–150				
J0849+5108 High	N	North_z20_average_50h	50	1000	20–150	3	50	1000	20–30, 30–50, 50–150
J0932+5306	N	North_z20_average_50h	50	100	20–150				
J0937+5008	N	North_z20_average_50h	50	100	20–150				
J0948+0022	N	North_z20_average_5h	3	1000	20–150	3	3	1000	20–30, 30–50, 50–150
("Flare" state)	S	South_z20_average_5h	3	1000	20–150	3	3	1000	20–30, 30–50, 50–150
	N	North_z20_average_5h	5	1000	20–150	3	5	1000	20–30, 30–50, 50–150
	S	South_z20_average_5h	5	1000	20–150	3	5	1000	20–30, 30–50, 50–150
	N	North_z20_average_5h	10	1000	20–150	3	10	1000	20–30, 30–50, 50–150
	S	South_z20_average_5h	10	1000	20–150	3	10	1000	20–30, 30–50, 50–150
J0948+0022	N	North_z20_average_5h	5	1000	20–150	3	5	1000	20–30, 30–50, 50–150
(High state)	S	South_z20_average_5h	5	1000	20–150	3	5	1000	20–30, 30–50, 50–150
	N	North_z20_average_5h	10	1000	20–150	3	10	1000	20–30, 30–50, 50–150
	S	South_z20_average_5h	10	1000	20–150	3	10	1000	20–30, 30–50, 50–150
	N	North_z20_average_50h	50	1000	20–150	4	50	1000	20–30, 30–50, 50–150, 20–50
	S	South_z20_average_50h	50	1000	20–150	4	50	1000	20–30, 30–50, 50–150, 20–50
J0948+0022	N	North_z20_average_50h	100	1000	20–150	1	100	1000	20–50
(Quiescent)	S	South_z20_average_50h	100	1000	20–150	1	100	1000	20–50
J0958+3224	N	North_z20_average_50h	50	100	20–150				
J1102+2239	N	North_z20_average_50h	50	100	20–150				
J1222+0413	N	North_z20_average_50h	50	100	20–150				
	S	South_z20_average_50h	50	100	20–150				
J1246+0238	N	North_z20_average_50h	50	100	20–150				
	S	South_z20_average_50h	50	100	20–150				
J1305+5116	N	North_z20_average_50h	50	100	20–150				
J1331+3030	N	North_z20_average_50h	50	100	20–150				
J1421+3855	N	North_z20_average_50h	50	100	20–150				
J1443+4725	N	North_z20_average_50h	50	100	20–150				
J1505+0326	N	North_z20_average_50h	50	100	20–150				
(Quiescent)	S	South_z20_average_50h	50	100	20–150				
J1520+4209	N	North_z20_average_50h	50	100	20–150				
J1641+3454	N	North_z20_average_50h	50	100	20–150				
J1644+2619 Flare	N	North_z20_average_5h	10	100	20–150				
(High)	N	North_z20_average_50h	50	100	20–150				
(Quiescent)	N	North_z20_average_50h	50	100	20–150				
J2007−4434	S	South_z20_average_50h	50	100	20–150				
J2118+0013	N	North_z20_average_50h	50	100	20–150				
	S	South_z20_average_50h	50	100	20–150				
J2118−0732	S	South_z20_average_50h	50	100	20–150				
No cut-off[b]									
J0849+5108 (High)	N	North_z20_average_5h				8	10	1000	20–30, 30–50, 50–75, 75–100, 100–140, 140–200, 200–300, 300–400
	N	North_z20_average_50h				8	50	1000	20–30, 30–50, 50–75, 75–100, 100–140, 140–200, 200–300, 300–400
J0849+5108 (Quiesc.)	N	North_z20_average_50h	100	1000	20–150	1	100	1000	20–50
J0948+0022	N	North_z20_average_5h	3	1000	20–150	8	3	1000	20–30, 30–50, 50–75, 75–100, 100–140, 140–200, 200–300, 300–400
("Flare" state)	S	South_z20_average_5h	3	1000	20–150	8	3	1000	20–30, 30–50, 50–75, 75–100, 100–140, 140–200, 200–300, 300–400
	N	North_z20_average_5h	5	1000	20–150	3	5	1000	20–30, 30–50, 50–150
	S	South_z20_average_5h	5	1000	20–150	3	5	1000	20–30, 30–50, 50–150
J0948+0022[b]	N	North_z20_average_5h	5	1000	20–150	8	5	1000	20–30, 30–50, 50–75, 75–100, 100–140, 140–200, 200–300, 300–400
(High state)	S	South_z20_average_5h	5	1000	20–150	8	5	1000	20–30, 30–50, 50–75, 75–100, 100–140, 140–200, 200–300, 300–400
J1505+0326	N	North_z20_average_5h				8	5	1000	20–30, 30–50, 50–75, 75–100, 100–140, 140–200, 200–300, 300–400
(High state)	S	South_z20_average_5h				8	5	1000	20–30, 30–50, 50–75, 75–100, 100–140, 140–200, 200–300, 300–400

[a] CTA site selected for the simulations: N=North (La Palma), S=South (Paranal).

[b] The input model did not include the cut-off due to internal absorption (see Sect. 5).

for the ranges of spectral parameters and exposures we considered. Therefore, after performing several test runs, we decided not to include the effects of energy dispersion in this exploratory work. As we show in Appendix A, given the exposure times selected and the resulting detection significance of our sources, we are confident that the effects are not significant enough to change our conclusions.

As a test case for relatively faint sources, we generally selected an exposure of 50 h, but considered exposures as short as 3 h for flaring states and as long as 100 h for quiescent states (details in Table 2, column 4). We note that 50 h correspond on average to the expected exposure that CTA can accumulate in one observing year on a single source, while 3–5 h correspond to the integration of 1–2 d, depending on source visibility and target scheduling.

In the following, we discuss details of the inputs for specific sources for which more than one flux state was considered.

J0849+5108 (SBS 0846+513). Two flux states were considered for this source. The high-state one [F2 flare (Paliya et al. 2016), integrated over 120 d] is modelled by means of a simple power-law model with photon index 2.10 and an integrated gamma-ray flux ($0.1 < E < 300$ GeV) of 9.92×10^{-8} ph cm^{-2} s^{-1}. The average flux state has been drawn from the FL8Y list, assuming a log-parabola spectrum (see FL8Y on-line FITS file for the spectral parameter) and an integrated gamma-ray flux ($1 < E < 100$ GeV) of 2.18×10^{-9} ph cm^{-2} s^{-1}. The high-state model was corrected for EBL absorption and intrinsic (BLR) absorption (cut-off at 30 GeV); the average-state model was corrected only for EBL.

J0948+0022 (PMN J0948+0022). Three flux states were considered for this source. The quiescent state [$F_{E>200\mathrm{MeV}} = (3.9 \pm 0.3) \times 10^{-8}$ ph cm^{-2} s^{-1}] was derived from Abdo et al. (2009a; integrating over 5 months), and is described by a broken power law with photon indices $\Gamma_1 = 2.3$ and $\Gamma_2 = 3.4$ and a break at 1 GeV. The high-state [$F_{E>100\mathrm{MeV}} = (1.02 \pm 0.02) \times 10^{-6}$ ph cm^{-2} s^{-1}] is described by a simple power-law model with photon index $\Gamma = 2.55$ (Foschini et al. 2011b). A third, flaring state was defined as three times brighter than the high state, with the same spectral shape. All models were corrected for EBL absorption and intrinsic (BLR) absorption (cut-off at 30 GeV).

FL8Y J1505.0+0326 (PKS 1502+036). We considered two flux states for this source, the quiescent state being derived from FL8Y. From D'Ammando et al. (2016b), instead, we drew a high state (as observed on 2015 December 20, 1 d integration) described by a power-law with a photon index $\Gamma = (2.54 \pm 0.04)$ and a flux $F_{0.1<E<300\mathrm{GeV}} = (93 \pm 19) \times 10^{-8}$ ph cm^{-2} s^{-1}. For this particular flare, we assume, as also concluded by D'Ammando et al. (2016b), based on the observed 3-week delay between the γ and radio light curve (15 GHz) peaks, that the dissipation region may lie outside the BLR. Therefore, no cut-off was applied to the input model for our simulations of the high state, while the average-state model was corrected for EBL absorption and intrinsic (BLR) absorption (cut-off at 30 GeV).

J1644+2619 (FBQS J1644.9 + 2619). Three flux states were considered for this source, the quiescent state being derived from FL8Y. From D'Ammando et al. (2015b), instead we drew a high state as an average over 2012 July 15 to October 12, described by a power law with a photon index $\Gamma = (2.5 \pm 0.2)$ and a flux $F_{0.1<E<100\mathrm{GeV}} = (5.2 \pm 1.0) \times 10^{-8}$ ph cm^{-2} s^{-1} and a flaring state as a daily average obtained on 2012 August 18 (MJD 56157) with a flux $F_{0.1<E<100\mathrm{GeV}} = (66 \pm 22) \times 10^{-8}$ ph cm^{-2} s^{-1}. For the sake of simplicity, we assumed for this flaring state the same photon index reported for the high state. All models were corrected for EBL absorption and intrinsic (BLR) absorption (cut-off at 30 GeV).

3.1 Detectability

A first set of simulations was dedicated to ascertaining whether the sources would be detectable by CTA. The general set-up is summarized in Table 2. In the following, we shall consider the reliability of a source detection in an energy band based on the test statistic (TS; Cash 1979; Mattox et al. 1996) of the maximum likelihood model fitting. In particular, the detection will have a high significance when TS $\geq$ 25 (Mattox et al. 1996) and a low significance when $10 \leq$ TS < 25. The source will not be considered detected for TS < 10 and an upper limit will need to be calculated instead.

Given the spectral softness of NLS1s, to investigate their detectability we selected a soft energy band, 20–150 GeV, in which the LSTs provide the full system sensitivity. In this band, we used the task `ctobssim` to create event lists based on our input models, including the randomized background events. We then used the task `ctlike` to fit a power-law model $M_{\mathrm{spectral}}(E) = k_0 \left(\frac{E}{E_0}\right)^{\Gamma}$, where k_0 is the normalization (or `Prefactor`, in units of ph cm^{-2} s^{-1} MeV^{-1}), E_0 is the pivot energy (`PivotEnergy` in MeV), and Γ is the power-law photon index (`Index`). In the fits, we left `Prefactor` and `Index` free to vary while we kept `PivotEnergy` fixed at 100 GeV. The task `ctlike` uses maximum likelihood model fitting and calculates TS.

To reduce the impact of variations between individual realizations (see e.g. Knödlseder et al. 2016), we performed sets of N (Table 2, column 5) statistically independent realizations by adopting different seeds (`seed`) for the randomization, where N was chosen as a compromise between accuracy in the assessment of the detection confidence level and computing time.[6] We thus obtained a set of N values of TS. We then derived the percentage of the detections for TS > 10 (Table 3, Col. 5) and the percentage of the detections for TS > 25 (Table 3, column 6). These represent the detection confidence levels. Then, the mean TS value and its uncertainty were calculated as the mean, $\overline{\mathrm{TS_{sim}}} = \frac{1}{N}\sum_{k=1}^{N} \mathrm{TS_{sim}}(k)$, and square root of the standard deviation of the sample of N values, $s^2_{\mathrm{sim}} = \frac{1}{N-1}\sum_{k=1}^{N}(\mathrm{TS_{sim}}(k) - \overline{\mathrm{TS_{sim}}})^2$. They are reported in Table 3 (column 7). For each realization, the best-fitting spectral parameters were used to calculate N values of flux in the 20–150 GeV energy band. Similarly, the flux mean and uncertainty were calculated and are reported in Table 3 (column 8). When the source was not detected, we calculated the 95 per cent confidence level upper limits on fluxes by using the task `ctulimit` (see Table 4). As inputs we used the first event file generated with `ctobssim` for which the task `ctlike` converged (TS > 0) and a model obtained by fitting the absorbed data with the log-parabola model.

3.2 Spectral properties

For the sources that were detected (Table 3), we then proceeded to investigate their spectral properties. We considered a set of M energy bins (Table 2, column 7) covering an energy band reported in Table 2 (column 10), namely soft (20–30 GeV), mid (30–50 GeV), softmid (20–50 GeV), and hard (50–150 GeV). In each bin, we used the task `ctobssim` to create event lists and then used the task `ctlike` to fit each spectral bin with a power-law model with the same set-up as for the detections (Section 3.1), with `PivotEnergy` fixed at

[6] In order to efficiently run such a large number of simulations, we performed them through Amazon Web Services, following the methods described in Landoni et al. (2018).

Table 3. Results of the first set of simulations (detections in the 20–150 GeV energy band), and the second set of simulations (detections in several bands). TS values and detection percentages and energy fluxes in each band.

Source name	CTA Site	Expo. (h)	Energy Range (GeV)	Det. c.l.[a] (TS > 10) (%)	Det. c.l.[a] (TS > 25) (%)	$\overline{TS_{sim}}$	E^2Flux[b] $\times 10^{-13}$ (erg cm^{-2} s^{-1})	Notes
J0849 + 5108	N	50	20–150	100.0	97.4	47.3 ± 13.8	10.6 ± 1.8	Fig. 1, Fig. 2
High state	N	50	20–30	78.7	13.1	16.4 ± 7.6	42.6 ± 12.6	
	N	50	30–50	94.5	37.7	22.7 ± 9.0	24.5 ± 5.7	
	N	50	50–150	74.6	12.4	15.5 ± 8.1	3.6 ± 1.5	
J0948+0022	N	3	20–150	95.8	59.4	28.4 ± 11.4	29.6 ± 8.9	
'Flare' state	S	3	20–150	97.0	73.5	32.9 ± 12.3	29.2 ± 7.9	
	N	3	20–30	63.8	6.1	13.3 ± 7.1	154.4 ± 52.1	
	S	3	20–30	71.5	9.7	14.9 ± 7.5	154.4 ± 48.8	
	N	3	30–50	63.5	6.7	13.3 ± 7.2	71.8 ± 24.3	
	S	3	30–50	73.0	11.3	15.3 ± 7.9	72.1 ± 23.2	
	N	3	50–150	23.6	0.6	6.9 ± 5.1	<30.7	
	S	3	50–150	30.8	1.0	7.8 ± 5.2	<16.8	
	N	5	20–150	99.6	95.7	45.8 ± 13.7	29.6 ± 6.1	
	S	5	20–150	99.7	98.2	53.4 ± 14.9	29.1 ± 5.5	
	N	5	20–30	90.7	30.3	21.0 ± 9.3	157.2 ± 40.5	
	S	5	20–30	94.6	39.6	23.6 ± 9.8	157.1 ± 37.3	
	N	5	30–50	90.0	28.6	20.8 ± 9.0	73.0 ± 19.2	
	S	5	30–50	94.8	43.7	24.4 ± 10.0	73.8 ± 17.6	
	N	5	50–150	39.7	2.1	9.5 ± 6.2	<20.3	
	S	5	50–150	56.0	4.4	11.6 ± 6.8	7.8 ± 4.2	
	N	10	20–150	100.0	100.0	89.2 ± 18.2	29.4 ± 4.2	Fig. 3, Fig. 6
	S	10	20–150	100.0	100.0	105.1 ± 20.5	29.2 ± 3.7	
	N	10	20–30	99.9	89.1	39.9 ± 12.7	159.4 ± 27.9	
	S	10	20–30	99.9	94.5	45.2 ± 13.8	159.6 ± 26.2	
	N	10	30–50	99.8	88.8	39.7 ± 12.2	74.1 ± 12.6	
	S	10	30–50	99.9	95.5	46.4 ± 13.4	74.3 ± 11.8	
	N	10	50–150	79.3	18.1	17.3 ± 8.9	8.0 ± 3.6	
	S	10	50–150	89.0	30.9	21.1 ± 9.7	7.7 ± 3.1	
J0948+ 0022	N	5	20–150	23.1	0.7	7.0 ± 5.1	<50.8	
High state	S	5	20–150	29.9	0.6	7.8 ± 5.2	<33.2	
	N	5	20–50	18.6	0.3	6.4 ± 4.6	<37.7	
	S	5	20–50	25.0	0.5	7.2 ± 5.1	<22.6	
	N	5	50–150	3.7	0.0	3.4 ± 3.1	<13.1	
	S	5	50–150	4.7	0.0	3.6 ± 3.1	<10.5	
	N	10	20–150	54.8	4.0	11.8 ± 6.8	9.7 ± 4.5	
	S	10	20–150	66.1	7.3	13.7 ± 7.3	9.8 ± 3.9	
	N	10	20–50	46.5	2.4	10.5 ± 6.2	32.8 ± 13.6	
	S	10	20–50	55.6	4.1	11.8 ± 6.6	33.1 ± 13.2	
	N	10	50–150	7.7	0.0	4.2 ± 3.5	<10.3	
	S	10	50–150	8.1	0.0	4.4 ± 3.6	<7.8	
	N	50	20–150	100.0	98.5	49.9 ± 14.2	9.7 ± 1.8	Fig. 4, Fig. 7
	S	50	20–150	100.0	100.0	59.3 ± 15.3	9.7 ± 1.6	
	N	50	20–30	94.8	38.7	23.5 ± 9.1	52.8 ± 12.1	
	S	50	20–30	97.6	51.5	26.4 ± 9.7	52.9 ± 11.4	
	N	50	30–50	94.2	37.8	22.8 ± 9.0	24.4 ± 5.7	
	S	50	30–50	97.3	54.2	26.9 ± 10.0	24.5 ± 5.2	
	N	50	50–150	47.6	3.2	10.7 ± 6.4	2.7 ± 1.4	
	S	50	50–150	63.5	7.7	13.5 ± 7.4	2.6 ± 1.3	
J0948+0022	N	100	20–150	93.3	29.1	21.4 ± 9.1	5.2 ± 1.3	Fig. 5
Quiescent	S	100	20–150	97.3	54.6	26.9 ± 10.2	5.3 ± 1.2	
	N	100	20–50	66.2	7.7	13.8 ± 7.4	12.2 ± 4.6	
	S	100	20–50	75.7	11.5	15.8 ± 7.8	12.5 ± 4.1	

[a]We consider a detection to have a high significance when TS $\geq$ 25 and a low significance when 10 $\leq$ TS < 25. The source will not be considered detected for TS < 10.

[b]Upper limits are calculated for the 95 per cent confidence level for all cases where TS < 10.

Table 4. Results of the first set of simulations (20–150 GeV energy band) and 95 per cent confidence level upper limit calculations.

Source name	CTA Site	Expo. (h)	Energy Range (GeV)	Det. c.l.[a] (TS>10) (%)	Det. c.l.[a] (TS>25) (%)	$\overline{TS_{sim}}$	E^2Flux[b] $\times10^{-13}$ (erg cm^{-2} s^{-1})	UL $\times10^{-13}$ (erg cm^{-2} s^{-1})
J0324+3410	N	50	20–150	0.0	0.0	1.7 ± 1.9	0.89 ± 0.97	<2.6
J0932+5306	N	50	20–150	0.0	0.0	2.0 ± 2.1	0.91 ± 0.97	<0.44
J0937+5008	N	50	20–150	0.0	0.0	1.9 ± 2.0	0.88 ± 0.94	<1.3
J0958+3224	N	50	20–150	0.0	0.0	1.8 ± 2.0	0.84 ± 0.96	<0.029
J1102+2239	N	50	20–150	0.0	0.0	2.0 ± 2.0	0.93 ± 0.98	<2.6
J1222+0413	N	50	20–150	0.0	0.0	1.8 ± 2.0	0.84 ± 0.95	<1.3
	S	50	20–150	1.9	0.0	2.3 ± 2.2	0.76 ± 0.77	<0.91
J1246+0238	N	50	20–150	0.0	0.0	1.8 ± 2.0	0.90 ± 0.96	<2.6
	S	50	20–150	2.0	0.0	2.2 ± 2.2	0.76 ± 0.76	<3.3
J1305+5116	N	50	20–150	0.0	0.0	2.0 ± 2.0	0.91 ± 0.96	<0.32
J1331+3030	N	50	20–150	0.0	0.0	1.8 ± 2.0	0.86 ± 0.96	<2.5
J1421+3855	N	50	20–150	0.0	0.0	1.9 ± 2.0	0.85 ± 0.96	<0.50
J1443+4725	N	50	20–150	0.0	0.0	2.0 ± 2.0	0.88 ± 0.96	<0.032
J1505+0326 quiescence	S	50	20–150	2.0	0.0	2.3 ± 2.2	0.89 ± 0.84	<5.6
J1520+4209	N	50	20–150	0.0	0.0	1.9 ± 2.0	0.88 ± 0.97	<1.8
J1641+3454	N	50	20–150	0.0	0.0	1.9 ± 2.0	0.94 ± 0.98	<0.34
J1644+2619 flare	N	10	20–150	34.1	0.0	8.8 ± 5.5	8.35 ± 4.41	<1.6
High	N	50	20–150	0.0	0.0	2.2 ± 2.2	1.14 ± 1.14	<0.70
Quiescence	N	50	20–150	0.0	0.0	2.0 ± 2.0	0.88 ± 0.95	<2.3
J2007−4434	S	50	20–150	1.8	0.0	2.1 ± 2.2	0.74 ± 0.76	<4.8
J2118+0013	S	50	20–150	2.0	0.0	2.2 ± 2.2	0.78 ± 0.76	<5.1
J2118−0732	S	50	20–150	2.2	0.0	2.0 ± 2.2	0.74 ± 0.75	<2.2

[a]We consider a detection to have a high significance when TS $\geq$ 25 and a low significance when 10 $\leq$ TS $<$ 25. The source will not be considered detected for TS $<$ 10.
[b]Upper limits are calculated for the 95 per cent confidence level for all cases where TS $<$ 10.

25 GeV for the soft band, 40 GeV for the mid band, 35 GeV for the softmid band, and 100 GeV for the hard band.

For each source, we obtained sets of N_2 realizations (Table 2, column 8). We then proceeded as in Section 3.1 and calculated average TS and spectral parameters and 95 per cent confidence level upper limits (see Table 4).

4 RESULTS

4.1 SBS 0846+513

Fig. 1a shows the distributions of the TS for SBS 0846+513 in the high state, in the full energy band (20–150 GeV), while Fig. 1(b–d) shows the distributions of the TS for the high state in the narrower energy bands. Table 3 reports the percentage of the detections for TS $>$ 10 and for TS $>$ 25 (columns 5 and 6), and the mean TS value (column 7) based on our simulations, as well as the mean flux in each of the energy bands we considered (column 8). We find that this source is

(i) detected in the high state (as described by Paliya et al. 2016) in 50 h (Fig. 2);
(ii) not detected in quiescence (FL8Y) in 100 h (even though no cut-off at 30 GeV representing internal absorption was applied; see Table 5).

4.2 PMN J0948+0022

In Figs 3, 4, and 5 (panels a), we plot the distributions of the TS for PMN J0948+0022 in the full energy band (20–150 GeV) while in the flaring, high, and quiescent states, respectively. In Figs 3, 4 (panels b, c, and d), and 5 (b), we plot the distributions of the TS for PMN J0948+0022 in the narrower bands in the flaring, high, and quiescent states. The percentages of the detections for TS $>$ 10 and for TS $>$ 25, mean TS and mean flux in each of the energy bands we considered can be found in Table 3.

This source, therefore, is

(i) detected in the 'flare' state in all bands in 10 h (Fig. 6);
(ii) detected in the 'flare' state up to 50 GeV in 3 h;
(iii) detected in the high state (as described by Foschini et al. 2011b) in all bands in 50 h (Fig. 7);
(iv) detected in high state up to 50 GeV in 10 h;
(v) detected in quiescence (as described by Abdo et al. 2009a) in the total band and softmid (20–50 GeV) band in 100 h.

4.3 PKS 1502+036

Since PKS 1502+036 was particularly bright during the high state, partly due to the fact that no cut-off at 30 GeV was applied, for the high state we performed a test for detection in 8 bands, extending up to 400 GeV (see Table 2). We find that this source is

(i) detected in the high state (as described by D'Ammando et al. 2016b) in 5 h in all bands up to 400 GeV (Fig. 8, Table 5); we note, again, that no cut-off at 30 GeV was applied in this case (see Section 3);
(ii) not detected in quiescence (FL8Y) in 100 h (Table 4).

4.4 Other sources

We investigated the possibility to detect all other sources in our sample in the 20–150 GeV energy band; however, no detections were obtained. The detailed results can be found in Table 4, which reports the percentage of the detections for *TS* $>$ 10 and for *TS* $>$ 25 (column 5, 6), and the mean TS value (column 7) based on our

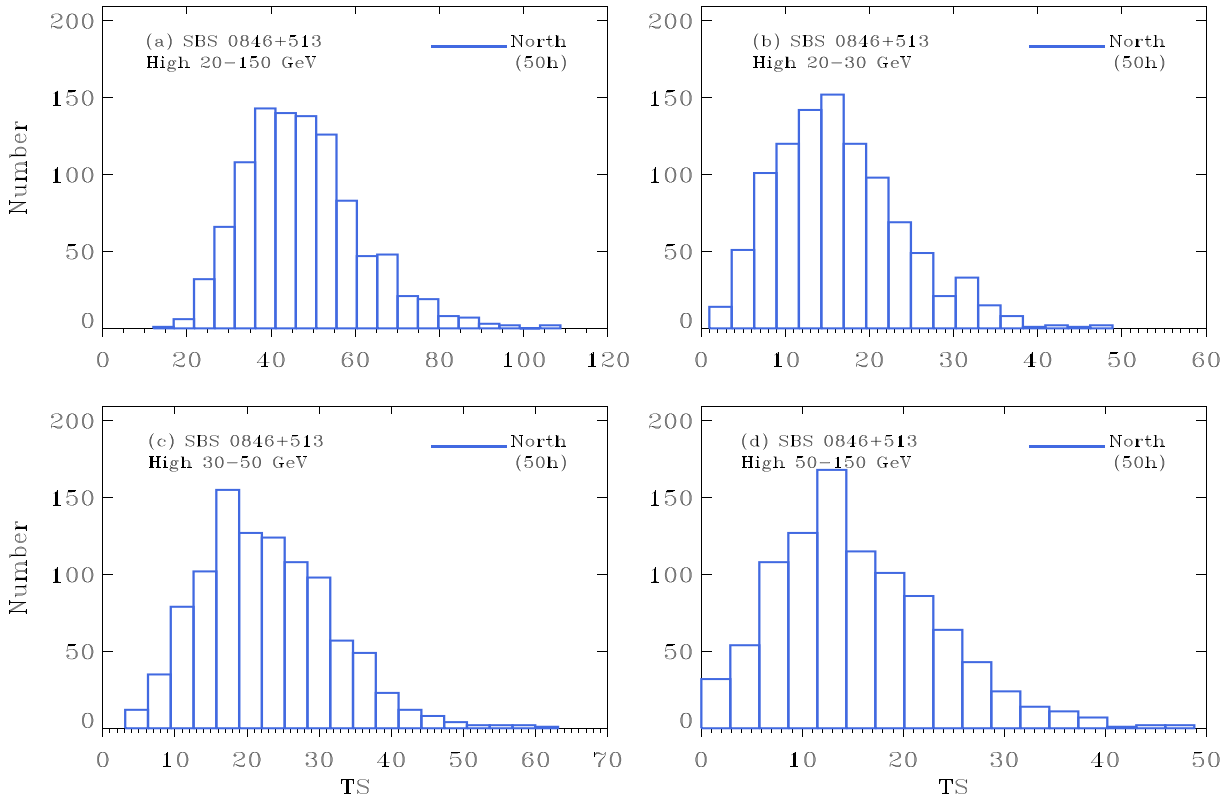

Figure 1. Distribution of the test statistic (TS) values for SBS 0846+513 in the high state in 50 h. See Table 3 for details.

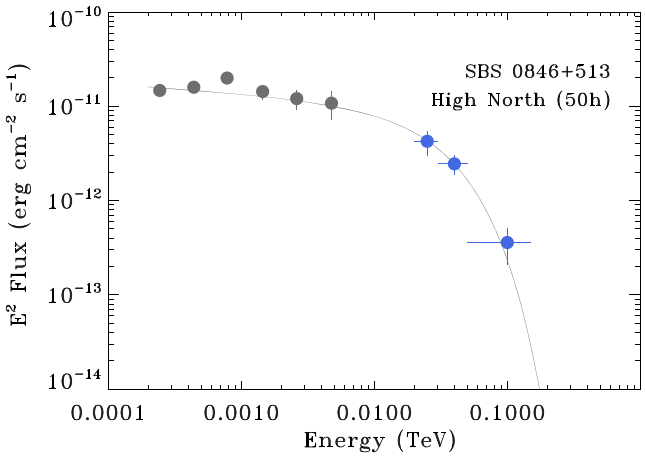

Figure 2. Spectral energy distribution (SED) of SBS 0846+513 in the high state. The grey line is the input model; the blue points are the simulated fluxes for 50 h of exposure. The grey points are from Paliya et al. (2016; F2 flare).

simulations, as well as the mean flux in each of the energy bands we considered (column 8). Column 9, finally, reports the 95 per cent upper limits on detection.

5 DISCUSSION

In this paper, we performed an investigation of the largest sample of γ-NLS1s to date, some in several flux states, in order to assess their suitability as potential CTA targets and to provide guidance in the possible observing strategy.

A first set of simulations was dedicated to ascertaining whether the sources would be detectable by CTA in the 'standard' framework in which one assumed that emission occurs at distances from the black hole (BH) smaller than the BLR radius (e.g. Abdo et al. 2009a). For each of the 20 sources, we simulated event files with `ctools` and performed a test for detection via the maximum likelihood method in the 20–150 GeV band, the most promising one due to the relative softness of these sources. The main assumptions for the input spectra were that they would need to be corrected for absorption by EBL (modelled according to Domínguez et al. 2011) and intrinsic absorption, which, for simplicity, has been modelled assuming an exponential cut-off at 30 GeV (see Section 3).

As expected, due to the faintness of γ-NLS1s, we did not detect most of the sample. However, three sources stood out as very promising, SBS 0846+513, PMN J0948+0022, and PKS 1502+036. We therefore investigated their spectral properties by performing a detection in several energy bands. SBS 0846+513 was detected in the high state, in 50 h, while PMN J0948+0022 was detected in the high state up to 150 GeV in 50 h and up to 50 GeV in 10 h. It was detected up to 150 GeV even in quiescence in 100 h. PKS 1502+036 was detected in all bands up to 400 GeV while in high state for which, we note, no cut-off was applied to the input model (D'Ammando et al. 2016b). This exploratory work, therefore, demonstrates that γ-NLS1s are indeed promising CTA targets even when the input spectra are heavily absorbed by EBL and intrinsic absorption. Furthermore, we note that the number of sources in our sample is still small, and their gamma-ray duty cycle not well known. This, combined with the large uncertainties in the input models (in particular the location of the dissipation region in each

Table 5. Results of the simulations of SBS 0846+513, PMN J0948+0022, and PKS 1502+036 with an input model that did not include the cut-off due to internal absorption (see Section 5).

Source name	CTA Site	Expo. (h)	Energy Range (GeV)	Det. c.l.[a] (TS>10) (%)	Det. c.l.[a] (TS>25) (%)	$\overline{TS_{sim}}$	E^2Flux[b] $\times10^{-13}$ (erg cm^{-2} s^{-1})	Notes
J0849+5108	N	10	20–30	100.0	100.0	76.5 ± 17.0	99.9 ± 11.9	Fig. 10
High state	N	10	30–50	100.0	100.0	299.1 ± 34.7	92.8 ± 5.8	
No cut-off	N	10	50–75	100.0	100.0	610.1 ± 50.4	82.7 ± 3.6	
	N	10	75–100	100.0	100.0	779.4 ± 58.4	71.8 ± 2.8	
	N	10	100–140	100.0	100.0	1133.8 ± 72.0	57.0 ± 1.9	
	N	10	140–200	100.0	100.0	1035.7 ± 70.7	35.9 ± 1.4	
	N	10	200–300	100.0	100.0	431.4 ± 46.0	14.5 ± 0.9	
	N	10	300–400	100.0	98.7	51.4 ± 14.5	4.1 ± 0.7	
J0849+5108	N	50	20–30	100.0	100.0	75.4 ± 16.6	99.8 ± 11.8	Fig. 9
High state	N	50	30–50	100.0	100.0	293.9 ± 33.5	92.8 ± 5.7	
No cut-off	N	50	50–75	100.0	100.0	605.8 ± 50.2	82.7 ± 3.7	
	N	50	75–100	100.0	100.0	770.5 ± 59.0	71.7 ± 2.9	
	N	50	100–140	100.0	100.0	1111.4 ± 74.4	57.0 ± 2.1	
	N	50	140–200	100.0	100.0	1044.6 ± 71.7	35.9 ± 1.4	
	N	50	200–300	100.0	100.0	447.3 ± 48.6	14.6 ± 1.0	
	N	50	300–400	100.0	98.6	53.2 ± 14.9	4.2 ± 0.7	
J0849+5108 quiescence	N	100	20–150	35.2	1.4	9.0 ± 5.7	<4.1	
No cut-off	N	100	20–50	13.3	0.0	5.4 ± 4.2	<9.2	
J0948+0022	N	3	20–30	100.0	99.5	58.9 ± 15.7	365.1 ± 52.4	Fig. 11
'Flare' state	S	3	20–30	100.0	100.0	67.1 ± 16.5	364.4 ± 49.0	
No cut-off	N	3	30–50	100.0	100.0	149.0 ± 25.3	277.4 ± 25.0	
	S	3	30–50	100.0	100.0	172.0 ± 28.0	277.4 ± 23.9	
	N	3	50–75	100.0	100.0	198.1 ± 30.1	201.0 ± 16.4	
	S	3	50–75	100.0	100.0	246.6 ± 33.9	201.0 ± 14.9	
	N	3	75–100	100.0	100.0	187.1 ± 29.7	150.0 ± 13.1	
	S	3	75–100	100.0	100.0	228.4 ± 33.1	150.0 ± 12.1	
	N	3	100–140	100.0	100.0	204.8 ± 32.5	103.2 ± 9.3	
	S	3	100–140	100.0	100.0	261.9 ± 36.8	103.5 ± 8.3	
	N	3	140–200	100.0	100.0	140.1 ± 27.2	55.3 ± 6.4	
	S	3	140–200	100.0	100.0	186.0 ± 33.4	55.5 ± 6.0	
	N	3	200–300	100.0	94.0	46.3 ± 15.4	18.8 ± 4.1	
	S	3	200–300	100.0	99.8	68.4 ± 17.7	18.7 ± 3.2	
	N	3	300–400	19.9	0.7	5.5 ± 5.1	<1.3	
	S	3	300–400	33.8	1.5	8.0 ± 6.2[c]	4.7 ± 2.4	
	N	5	20–150	100.0	100.0	1362.3 ± 80.6	207.3 ± 6.7	
	S	5	20–150	100.0	100.0	1677.6 ± 87.6	207.3 ± 6.1	
	N	5	20–30	100.0	100.0	96.5 ± 19.8	366.1 ± 40.0	
	S	5	20–30	100.0	100.0	110.7 ± 21.0	366.1 ± 37.0	
	N	5	30–50	100.0	100.0	246.2 ± 32.7	277.3 ± 19.7	
	S	5	30–50	100.0	100.0	285.6 ± 36.1	277.7 ± 18.6	
	N	5	50–150	100.0	100.0	1026.4 ± 69.0	143.1 ± 5.3	
	S	5	50–150	100.0	100.0	1288.1 ± 83.7	142.9 ± 4.8	
J0948+0022	N	5	20–30	60.8	7.6	13.1 ± 7.2	117.6 ± 40.2	Fig. 12
High state	S	5	20–30	69.6	9.2	14.6 ± 7.5	117.2 ± 37.9	
No cut-off	N	5	30–50	98.8	66.3	30.6 ± 11.0	91.1 ± 18.8	
	S	5	30–50	99.7	80.7	35.7 ± 12.1	91.6 ± 17.4	
	N	5	50–75	99.9	91.5	42.3 ± 13.5	66.5 ± 11.7	
	S	5	50–75	100.0	98.6	52.7 ± 14.8	66.4 ± 10.1	
	N	5	75–100	100.0	88.9	40.9 ± 13.2	49.4 ± 8.8	
	S	5	75–100	100.0	97.9	50.8 ± 14.9	49.5 ± 8.0	
	N	5	100–140	99.9	94.1	45.8 ± 14.2	33.9 ± 5.9	
	S	5	100–140	100.0	99.3	59.9 ± 16.3	34.2 ± 5.2	
	N	5	140–200	98.7	73.0	33.0 ± 12.3	18.2 ± 4.0	
	S	5	140–200	99.9	93.0	44.5 ± 14.3	18.3 ± 3.4	
J0948+0022	N	5	200–300	53.1	5.3	11.8 ± 7.1	6.2 ± 2.6	
High state	S	5	200–300	78.9	17.7	17.5 ± 9.0	6.2 ± 2.1	
No cut-off	N	5	300–400	4.5	0.0	3.1 ± 3.0	<0.72	
	S	5	300–400	5.7	0.0	3.6 ± 3.3	<0.59	
	N	5	20–150	100.0	100.0	171.0 ± 27.0	69.1 ± 6.1	

Table 5 – *continued*

Source name	CTA Site	Expo. (h)	Energy Range (GeV)	Det. c.l.[a] (TS>10) (%)	Det. c.l.[a] (TS>25) (%)	$\overline{\mathrm{TS_{sim}}}$	E^2Flux[b] $\times 10^{-13}$ (erg cm^{-2} s^{-1})	Notes
	S	5	20–150	100.0	100.0	213.8 ± 29.7	69.1 ± 5.5	
	N	5	50–150	100.0	100.0	132.7 ± 24.6	47.7 ± 4.7	
	S	5	50–150	100.0	100.0	169.5 ± 27.8	47.6 ± 4.2	
J1505+0326	N	5	20–30	55.7	5.4	12.2 ± 6.9	112.4 ± 39.9	Fig. 8
High state	S	5	20–30	64.9	8.3	13.7 ± 7.3	112.7 ± 38.1	
No cut-off	N	5	30–50	98.5	62.2	29.5 ± 10.8	89.3 ± 18.9	
	S	5	30–50	99.4	78.1	34.5 ± 12.0	89.7 ± 17.7	
	N	5	50–75	99.9	93.5	43.9 ± 13.6	67.8 ± 11.5	
	S	5	50–75	100.0	99.1	54.8 ± 14.9	67.7 ± 10.1	
	N	5	75–100	100.0	94.4	46.2 ± 14.2	52.8 ± 8.9	
	S	5	75–100	100.0	99.3	57.3 ± 15.8	52.9 ± 8.0	
	N	5	100–140	100.0	99.8	61.8 ± 16.5	40.2 ± 5.9	
	S	5	100–140	100.0	100.0	80.6 ± 18.9	40.3 ± 5.3	
	N	5	140–200	100.0	99.7	60.2 ± 16.2	26.1 ± 4.0	
	S	5	140–200	100.0	100.0	80.9 ± 19.9	26.1 ± 3.7	
	N	5	200–300	99.5	74.0	34.3 ± 12.9	12.5 ± 2.9	
	S	5	200–300	100.0	97.1	52.2 ± 16.2	12.6 ± 2.3	
	N	5	300–400	34.0	1.6	8.5 ± 6.1	4.9 ± 2.4	
	S	5	300–400	54.7	6.5	12.2 ± 7.5	4.8 ± 2.0	

[a]Significance for the detection is high for TS $\geq$ 25, low for 10 $\leq$ TS $<$ 25; source not detected for TS $<$ 10.
[b]Upper limits are calculated for the 95 per cent confidence level for all cases where TS $<$ 10.
[c]Tentative detection based on 1000 realizations.

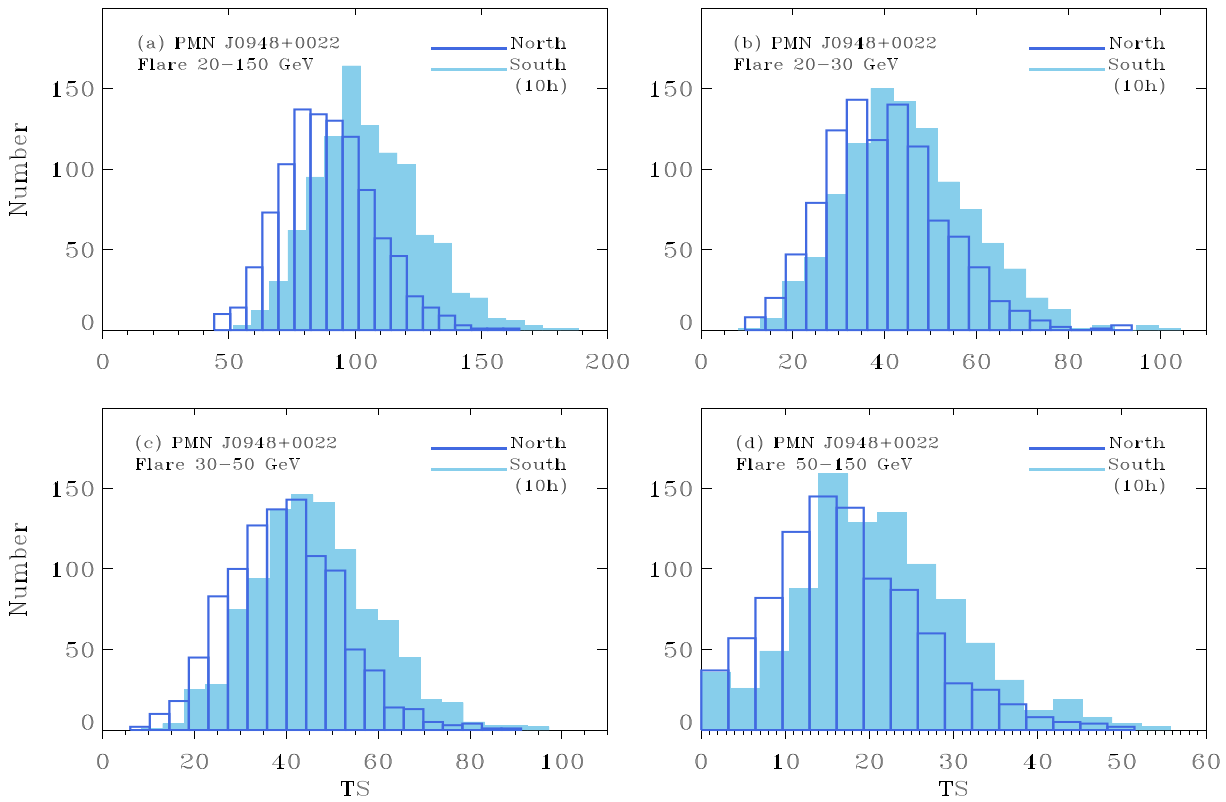

Figure 3. Distribution of the TS values for PMN J0948+0022 in the 'flare' state in 10 h. See Table 3 for details. The systematic shift in the TS distribution to larger mean TS values for the south is related to the slightly larger sensitivity of the South array with respect to the North array (see https://www.cta-observatory.org/science/cta-performance).

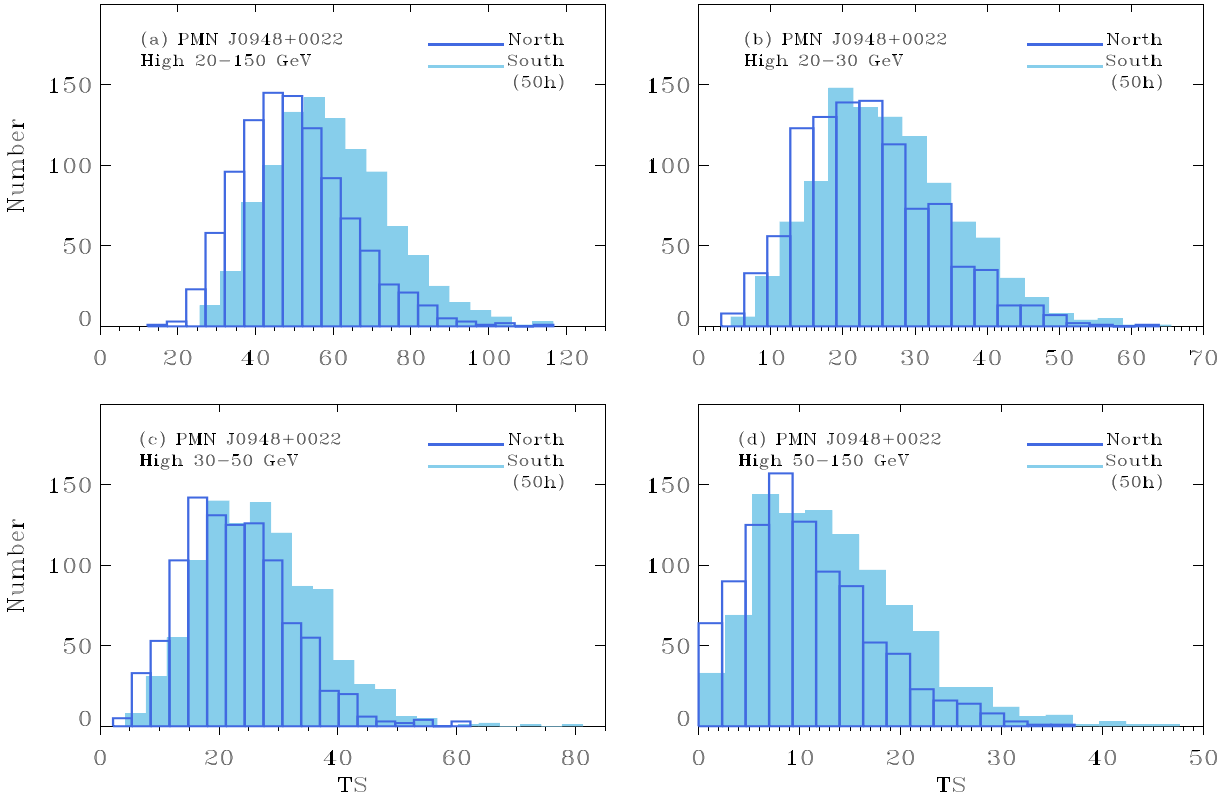

Figure 4. Distribution of the TS values for PMN J0948+0022 in the high state in 50 h. See Table 3 for details.

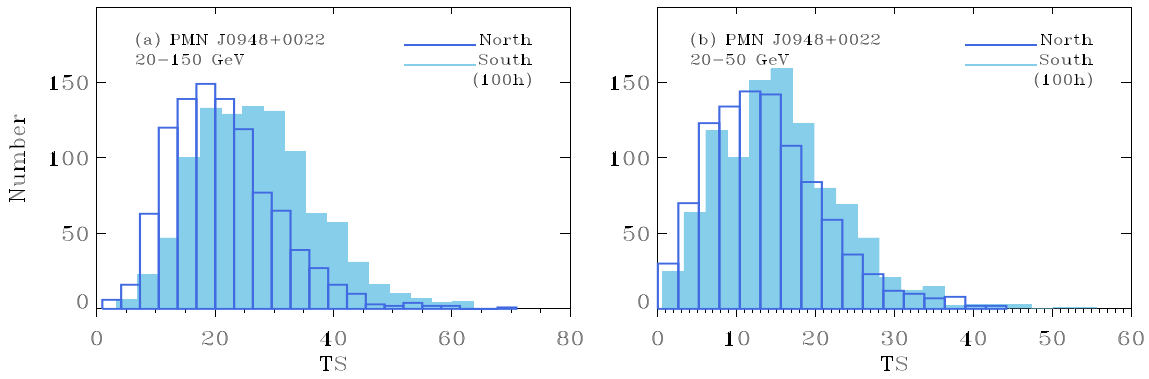

Figure 5. Distribution of the TS values for PMN J0948+0022 in the quiescent state in 100 h. See Table 3 for details.

flare; see below, and in D'Ammando et al. 2015a, and references therein), may increase the fraction of NLS1s detected in the CTA bands.

Evidence is emerging that for blazars the location of the gamma-ray-emitting region may not always be placed at the same distance from the central BH during different flaring episodes of the same source as suggested by e.g. Foschini et al. (2011a) for PKS 1222+216 [and subsequently by e.g. Brown (2013), for PKS 1510-089, Coogan, Brown & Chadwick (2016) and Finke (2016) for 3C 454.3]. This is especially supported by the absence in some FSRQs of the expected spectral breaks/cut-off (Abeysekara et al. 2015; Costamante et al. 2018, and references therein) at 20–30 GeV expected to mark the absorption of the gamma-rays with the UV radiation emitted by the BLR clouds (e.g. Poutanen & Stern 2010). It is also supported by the detection of seven FSRQs in the VHE band (MAGIC Collaboration 2008; Neronov, Semikoz & Vovk 2010; Aleksić et al. 2011; H.E.S.S. Collaboration 2013; Ahnen et al. 2015; Abeysekara et al. 2015; Sitarek et al. 2015; Cerruti et al. 2017; Mirzoyan 2017; Mukherjee & VERITAS Collaboration 2017; also see TeVCat[7] for further references). Support to this also comes from the dramatic change of the position of the synchrotron and inverse Compton peaks for some FSRQs during extreme flares (Ghisellini et al. 2013; Pacciani et al. 2014; Ahnen et al. 2015), interpreted as due to the smaller cooling suffered by the electrons in the less dense radiation field outside the BLR. In fact, the lower cooling would allow the acceleration mechanism to push the electrons at larger energies, determining the shift of the spectral peaks to larger frequencies.

[7] http://tevcat.uchicago.edu/.

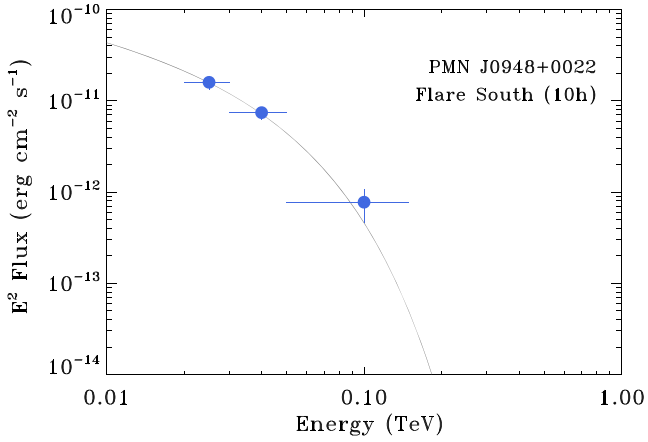

Figure 6. SED of PMN J0948+0022 in flare. The grey line is the input model; the blue points are the simulated fluxes (10 h exposure).

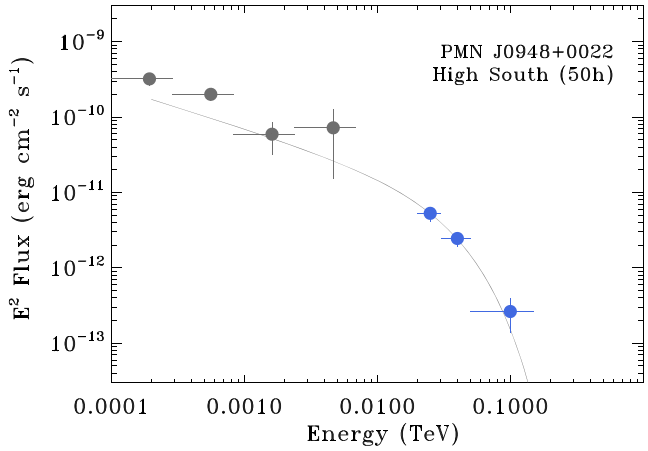

Figure 7. SED of PMN J0948+0022 in the high state. The grey line is the input model; the blue points are the simulated fluxes (50 h exposure). The grey points are from Foschini et al. (2011b).

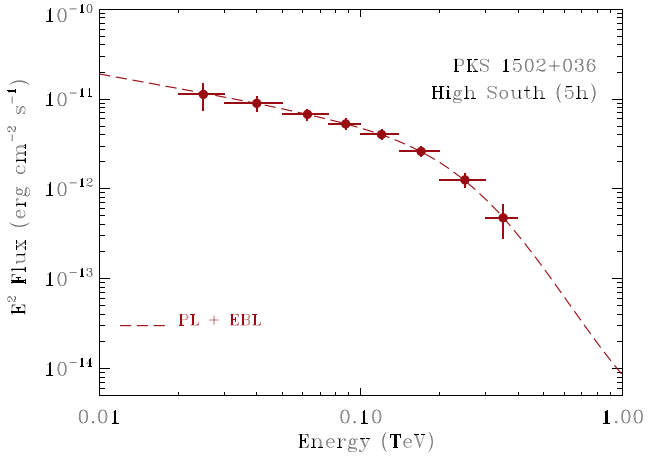

Figure 8. SED of PKS 1502+036 in the high state for an exposure of 5 h. The red dashed line is the input model which does not include the cut-off due to internal absorption; the red points are the simulated fluxes (Table 5).

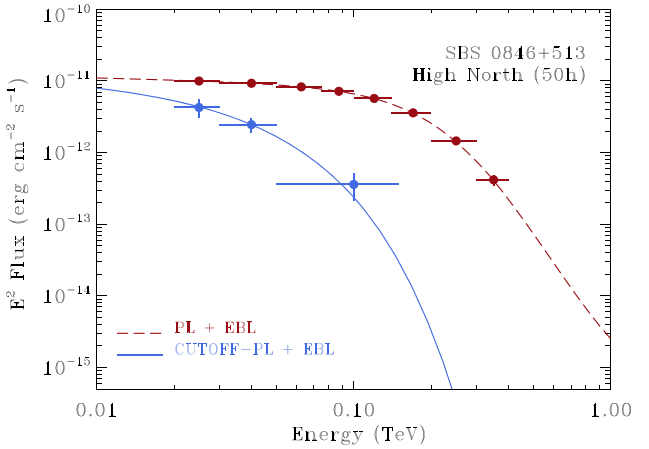

Figure 9. SED of SBS 0846+513 in the high state (exposure of 50 h). The blue line is the input model (see Section 2); the blue points are the simulated fluxes (Table 3). The red dashed line is the input model that does not include the cut-off due to internal absorption; the red points are the simulated fluxes (Table 5).

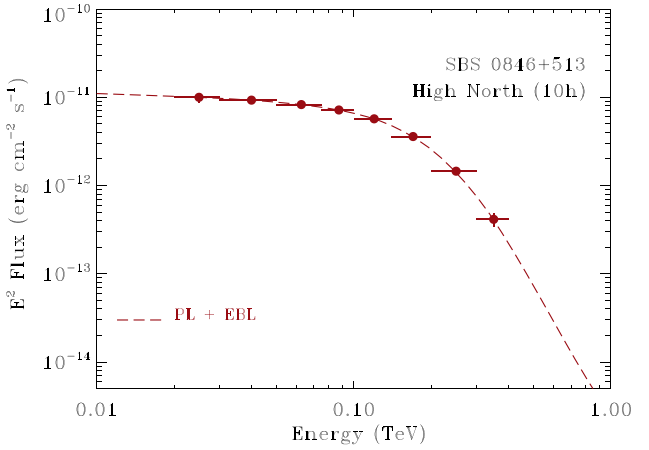

Figure 10. SED of SBS 0846+513 in the high state for an exposure of 10 h. The red dashed line is the input model that does not include the cut-off due to internal absorption; the red points are the simulated fluxes (Table 5).

Due to the close similarity between blazars and NLS1s, it is conceivable that the phenomenology discussed above can also be displayed by NLS1s. We therefore investigated the impact of the position of the emitting region on the detectability for the prototypical sources SBS 0846+513 and PMN J0948+0022 by simulating a further model, in addition to those described in Section 3 (the latter included both attenuation due to the EBL and an internal absorption exponential cut-off, with the exception of the high state of PKS 1502+036), assuming that the spectrum can extend unbroken above 20–30 GeV. The simulation set-up is reported at the bottom of Table 2, the results in Table 5.

Fig. 9 shows the comparison of these two models for the high state of SBS 0846+513 in 50 h, with the blue solid line representing the cut-off + EBL model and simulated fluxes (from Table 3) and the red dashed line representing the input model that does not include the cut-off due to internal absorption and the simulated fluxes (Table 5). Given the high TS obtained for each band in the latter model, we also simulated a 10 h exposure (see Fig. 10). It was done similarly for PMN J0948+0022, for both the 'flare' state in 3 h (Fig. 11) and the high state in 5 h (Fig. 12).

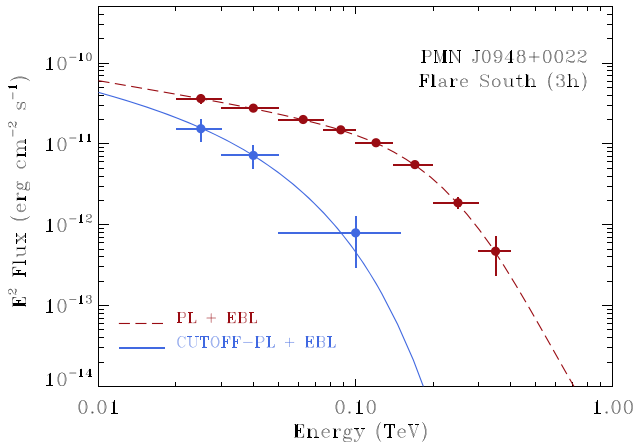

Figure 11. SED of PMN J0948+0022 in flare (exposure of 3 h). The blue line is the input model (see Section 2); the blue points are the simulated fluxes (Table 3). The red dashed line is the input model that does not include the cut-off due to internal absorption; the red points are the simulated fluxes (Table 5).

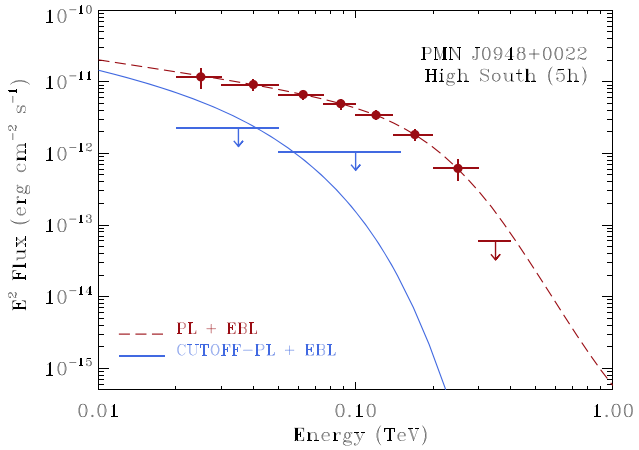

Figure 12. Same as Fig. 11 for the SED of PMN J0948+0022 in the high state (exposure of 5 h).

Figs 11 and 12 clearly show that for high gamma-ray emission states in 5 h of observations, CTA will be able to discriminate between the two competing models, providing strong constraints on the location of the jet-dissipation region. For more intense gamma-ray activity (flaring state), 3 h of observation should allow us to perform time-selected spectroscopy of the gamma-ray event. We note, however, that in a more realistic situation we can expect that the spectrum, assumed here to be a power law with the same slope up to 1 TeV, will display a progressive softening with energy [as expected, for instance, because of the transition of the inverse Compton (IC) scattering from the Thomson to the Klein–Nishina regime]. This would have an important impact on the observed spectra, in particular at the highest energies.

γ-NLS1s are known to be quite variable on time-scales of hours to days, time-scales in which CTA has a distinct advantage over *Fermi*-LAT in the 20–200 GeV band.[8] γ-NLS1s, therefore, turn out to be excellent targets for observations in response to triggers from other facilities. As detailed in Cherenkov Telescope Array Consortium (2018), Bulgarelli et al. (2015), and Fioretti et al. (2015), as a requirement, CTA will be able to repoint an external trigger in less than 50 s. In such cases, CTA will be able to detect and obtain detailed spectra in a few hours for flaring states, and in a day or so for high states (see Figs 8 and 10).

In the unfortunate circumstances of an interruption of the scientific activity of the current wide-FOV gamma-ray satellites (AGILE and *Fermi*-LAT) in combination with the possible absence of the e-ASTROGAM mission (De Angelis et al. 2017) during the CTA science phase, studying NLS1 galaxies with CTA clearly becomes paramount. In particular, the optimal combination of LSTs and MSTs will allow us to investigate such sources from a few tens up to a few hundred GeV, providing discriminating information on the location of the gamma-ray-emitting region.

[8] www.cta-observatory.org/science/cta-performance/ #1525680063092-06388df6-d2af.

ACKNOWLEDGEMENTS

We thank R.L.C. Starling and F. D'Ammando for helpful discussions, and M. Böttcher, M. Tornikoski, and J. Biteau as internal CTA reviewers.

The authors acknowledge contribution from the grant INAF CTA–SKA, 'Probing particle acceleration and γ-ray propagation with CTA and its precursors' (PI F. Tavecchio).

This research has made use of the NASA/IPAC Extragalactic Database (NED) which is operated by the Jet Propulsion Laboratory, California Institute of Technology, under contract with the National Aeronautics and Space Administration.This research made use of `ctools`, a community-developed analysis package for Imaging Air Cherenkov Telescope data. ctools is based on `GammaLib`, a community-developed toolbox for the high-level analysis of astronomical gamma-ray data. This research has made use of the CTA instrument response functions provided by the CTA Consortium and Observatory; see https://www.cta-observatory.org/science/cta-performance/ (version prod3b-v1) for more details.

We gratefully acknowledge financial support from the agencies and organizations listed here: http://www.cta-observatory.org/consortium_acknowledgments. This paper went through internal review by the CTA Consortium.

We also thank the anonymous referee for swift comments that helped improve the paper.

REFERENCES

Abdo A. A. et al., 2009a, ApJ, 699, 976
Abdo A. A. et al., 2009b, ApJ, 707, 727
Abeysekara A. U. et al., 2015, ApJ, 815, L22
Acharya B. S. et al., 2013, Astropart. Phys., 43, 3
Actis M. et al., 2011, Exp. Astron., 32, 193
Ahnen M. L. et al., 2015, ApJ, 815, L23
Aleksić J. et al., 2011, ApJ, 730, L8
Berton M. et al., 2017, Frontiers in Astronomy and Space Sciences, 4, 8
Boller T., Brandt W. N., Fink H., 1996, A&A, 305, 53
Brown A. M., 2013, MNRAS, 431, 824
Bulgarelli A. et al., 2015, in Borisov A. S. et al., eds, Proc. Sci., The On-Site Analysis of the Cherenkov Telescope Array, SISSA, Trieste, PoS(ICRC2015)7, http://pos.sissa.it/cgi-bin/reader/conf.cgi?confid=236
Cash W., 1979, ApJ, 228, 939
Cerruti M., Lenain J.-P., Prokoph H. for the H. E. S. S. Collaboration, 2017, H.E.S.S. discovery of very-high-energy emission from the blazar PKS 0736+017: on the location of the γ-ray emitting region in FSRQs.

SISSA, Trieste, PoS(ICRC2017)627, http://pos.sissa.it/cgi-bin/reader/conf.cgi?confid=301
Cherenkov Telescope Array Consortium, 2018, Science with the Cherenkov Telescope Array, World Scientific, preprint (arXiv:1709.07997)
Coogan R. T., Brown A. M., Chadwick P. M., 2016, MNRAS, 458, 354
Costamante L., Cutini S., Tosti G., Antolini E., Tramacere A., 2018, MNRAS, 477, 4749
Cracco V., Ciroi S., Berton M., Di Mille F., Foschini L., La Mura G., Rafanelli P., 2016, MNRAS, 462, 1256
Crenshaw D. M., Kraemer S. B., Gabel J. R., 2003, AJ, 126, 1690
D'Ammando F. et al., 2015a, MNRAS, 446, 2456
D'Ammando F., Orienti M., Larsson J., Giroletti M., 2015b, MNRAS, 452, 520
D'Ammando F., Orienti M., Finke J., Larsson J., Giroletti M., Raiteri C., 2016a, Galaxies, 4, 11
D'Ammando F. et al., 2016b, MNRAS, 463, 4469
De Angelis A. et al., 2017, Exp. Astron., 44, 25
Domínguez A. et al., 2011, MNRAS, 410, 2556
Falcone A. D. et al., 2004, ApJ, 613, 710
Finke J. D., 2016, ApJ, 830, 94
Fioretti V., Bulgarelli A., Zoli A., Markoff S., Ribó M., Inoue S., Grandi P., De Cesare G., 2015, in Borisov A. S. et al., eds, Proc. Sci., Real-Time Analysis sensitivity evaluation of the Cherenkov Telescope Array. SISSA, Trieste, PoS(ICRC2015)699, http://pos.sissa.it/cgi-bin/reader/conf.cgi?confid=236
Foschini L., 2011, in Foschini L., Colpi M., Gallo L., Grupe D., Komossa S., Leighly K., Mathur S., eds, Proc. Sci., Evidence of powerful relativistic jets in narrow-line Seyfert 1 galaxies, SISSA, Trieste, PoS(NLS1)024, http://pos.sissa.it/cgi-bin/reader/conf.cgi?confid=126
Foschini L., 2012, Proc. Sci., Powerful relativistic jets in narrow-line Seyfert 1 glaxies (review) , SISSA, Trieste, PoS(Seyfert 2012)010, http://pos.sissa.it/cgi-bin/reader/conf.cgi?confid=169
Foschini L., Maraschi L., Tavecchio F., Ghisellini G., Gliozzi M., Sambruna R. M., 2009, Adv. Space Res., 43, 889
Foschini L. Fermi/Lat Collaboration Ghisellini G., Maraschi L., Tavecchio F., Angelakis E., 2010, in Maraschi L., Ghisellini G., Della Ceca R., Tavecchio F., eds, ASP Conf. Ser. Vol 427, Accretion and Ejection in AGN: A Global View. Astron. Soc. Pac., San Francisco, p. 243
Foschini L., Ghisellini G., Tavecchio F., Bonnoli G., Stamerra A., 2011a, in Morselli A.., eds, Proc. 2011 Fermi Symp. eConf C110509, preprint (arXiv:1110.5649)
Foschini L. et al., 2011b, MNRAS, 413, 1671
Foschini L. et al., 2015, A&A, 575, A13
Ghisellini G., Tavecchio F., Foschini L., Bonnoli G., Tagliaferri G., 2013, MNRAS, 432, L66
Goodrich R. W., 1989, ApJ, 342, 224
H.E.S.S. Collaboration, 2013, A&A, 554, A107
H. E. S. S. Collaboration, 2014, A&A, 564, A9
Hofmann W., 2017a, The Messenger, 168, 21
Hofmann W., 2017b, in Aharonian F. A., Hofman W., Rieger F. M., eds, AIP Conf. Proc. 1792, 6th International Symposium on High Energy Gamma-Ray Astronomy. Am. Inst. Phys., New York, p. 020014
Knödlseder J. et al., 2016, A&A, 593, A1
Komossa S., Voges W., Xu D., Mathur S., Adorf H.-M., Lemson G., Duschl W. J., Grupe D., 2006, AJ, 132, 531
Lähteenmäki A. et al., 2017, A&A, 603, A100
Lähteenmäki A., Järvelä E., Ramakrishnan V., Tornikoski M., Tammi J., Vera R. J. C., Chamani W., 2018, A&A, 614, L1
Landoni M., Romano P., Vercellone S., Knödlseder J., Bianco A., Tavecchio F., Corina A., 2018, ApJS, submitted
Liao N.-H., Liang Y.-F., Weng S.-S., Berton M., Gu M.-F., Fan Y.-Z., 2015, preprint (arXiv:1510.05584)
MAGIC Collaboration, 2008, Science, 320, 1752
Maier G., Arrabito L., Bernlöhr K., Bregeon J., Cumani P., Hassan T., Moralejo A., 2017, Performance of the Cherenkov Telescope Array, SISSA, Trieste, PoS(ICRC2017)846, http://pos.sissa.it/cgi-bin/reader/conf.cgi?confid=301
Mattox J. R. et al., 1996, ApJ, 461, 396
Mirzoyan R., 2017, ATel, 11061
Mukherjee R. VERITAS Collaboration, 2017, ATel, 11075
Neronov A., Semikoz D., Vovk I., 2010, ATel, 2617
Oshlack A. Y. K. N., Webster R. L., Whiting M. T., 2001, ApJ, 558, 578
Osterbrock D. E., Pogge R. W., 1985, ApJ, 297, 166
Pacciani L., Tavecchio F., Donnarumma I., Stamerra A., Carrasco L., Recillas E., Porras A., Uemura M., 2014, ApJ, 790, 45
Paliya V. S., Stalin C. S., Ravikumar C. D., 2015, AJ, 149, 41
Paliya V. S., Rajput B., Stalin C. S., Pandey S. B., 2016, ApJ, 819, 121
Paliya V. S., Ajello M., Rakshit S., Mandal A. K., Stalin C. S., Kaur A., Hartmann D., 2018, ApJ, 853, L2
Peterson B. M. et al., 2004, ApJ, 613, 682
Poutanen J., Stern B., 2010, ApJ, 717, L118
Sahakyan N., Baghmanyan V., Zargaryan D., 2018, A&A, 614, A6
Sitarek J. et al., 2015, in Borisov A. S. et al., eds, Proc. Sci., Detection of very-high-energy gamma rays from the most distant and gravitationally lensed blazar S3 0218+35 using the MAGIC t., SISSA, Trieste, PoS(ICRC2015), http://pos.sissa.it/cgi-bin/reader/conf.cgi?confid=236
Yao S., Yuan W., Zhou H., Komossa S., Zhang J., Qiao E., Liu B., 2015, MNRAS, 454, L16
Yuan W., Zhou H. Y., Komossa S., Dong X. B., Wang T. G., Lu H. L., Bai J. M., 2008, ApJ, 685, 801
Zhou H.-Y., Wang T.-G., Dong X.-B., Zhou Y.-Y., Li C., 2003, ApJ, 584, 147

APPENDIX A: EFFECT OF ENERGY DISPERSION

In the following, we address the effect of the energy dispersion on our conclusions by considering one exemplary source, PMN J0948+0022 in flare, as simulated in 5 h. The set-up of these new simulations, reported in Table A1, is the same as that of the earlier simulations performed for this source, with the exception of the application of energy dispersion. We note, however, that these simulations were performed with `ctools` v. 1.5.1 (as opposed to v. 1.4.2 as for the rest of this work), which removes any noise in the energy dispersion matrix that degraded the precision of the energy dispersion computations in earlier software versions.

Fig. A1 shows the comparison of the TS distributions for fits performed without (blue, top panels) and with (green, bottom panels) energy dispersion applied. Table A2 reports this comparison in terms of detection percentages, TS mean values, and derived energy fluxes in each band (columns 1–6). For ease of comparison, we also report (column 7) the corresponding TS mean values for the case

Table A1. Set-up ofthe (`ctools`) simulations to test effects of energy dispersion on PMN J0948+0022 in flare. CTA site selected for the simulations: N = North (La Palma), S = South (Paranal).

Site	IRF	Expo (h)	Sim. N_1	Energy (GeV)
N	`North_z20_average_5h`	5	1000	20–150
N	`North_z20_average_5h`	5	1000	20–30
N	`North_z20_average_5h`	5	1000	30–50
N	`North_z20_average_5h`	5	1000	50–150
S	`South_z20_average_5h`	5	1000	20–150
S	`South_z20_average_5h`	5	1000	20–30
S	`South_z20_average_5h`	5	1000	30–50
S	`South_z20_average_5h`	5	1000	50–150

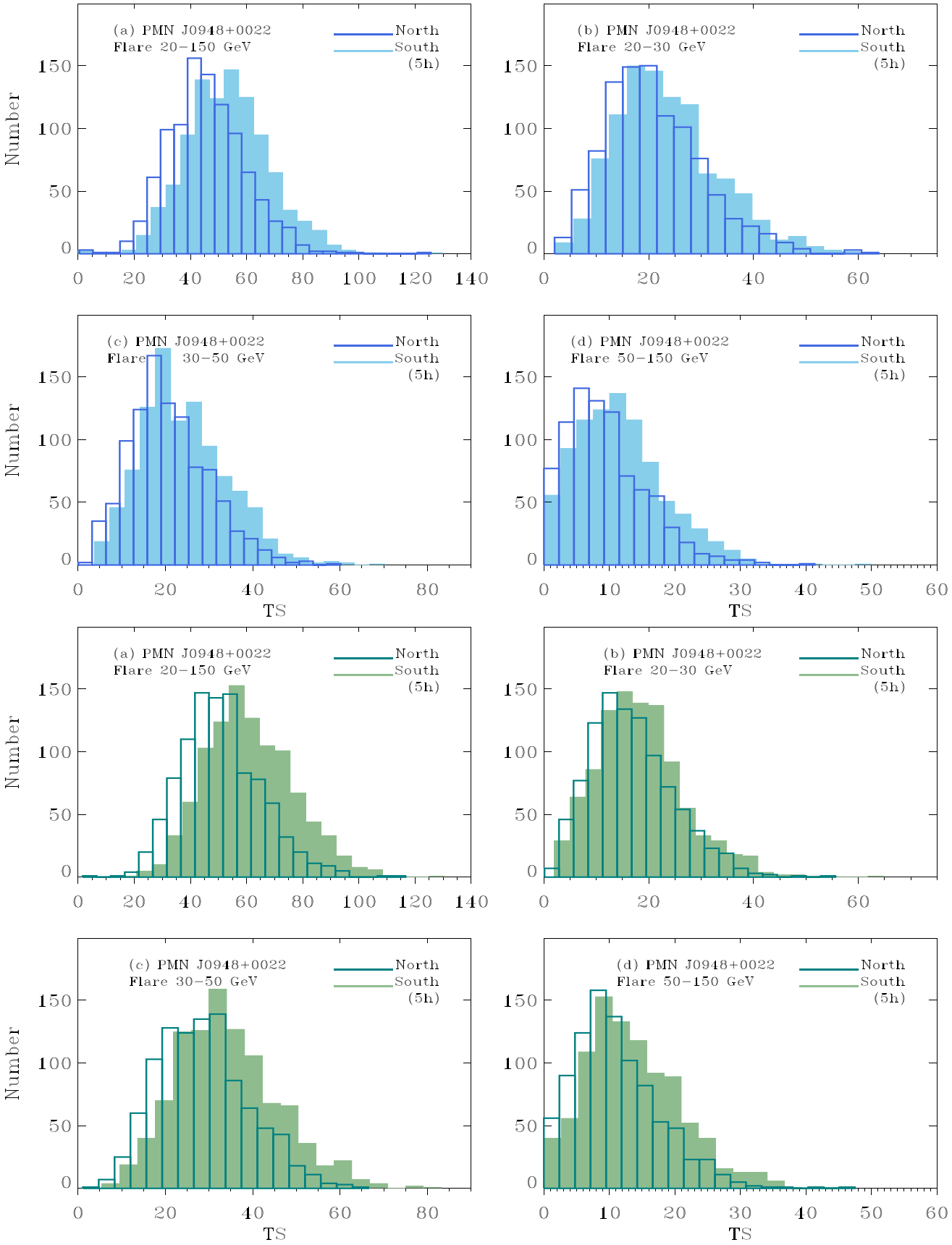

Figure A1. PMN J0948+0022 in 'flare' (exposure 5 h): comparison of distributions of the TS values depending on the energy band for detection. Blue: `edisp=no`, green: `edisp=yes`. See Table 3 and A1 for details.

Table A2. Results for PMN J0948+0022 in flare (5 h exposure) when energy dispersion is applied (columns 1–6), compared with the case when no energy dispersion is applied (column 7).

CTA Site	Energy Range (GeV)	Det. c.l. (TS > 10) (%)	Det. c.l. (TS > 25) (%)	$\overline{TS_{sim}}$	E^2Flux $\times 10^{-13}$ (erg cm^{-2} s^{-1})	$\overline{TS_{sim}}$[a] No energy Dispersion
N	20–150	99.9	98.2	50.9 ± 14.3	29.0 ± 6.1	45.8 ± 13.7
S	20–150	100.0	99.7	61.0 ± 15.6	28.7 ± 5.3	53.4 ± 14.9
N	20–30	80.7	15.1	16.8 ± 7.9	110.3 ± 56.3	21.0 ± 9.3
S	20–30	85.6	19.2	18.5 ± 8.5	112.4 ± 54.2	23.6 ± 9.8
N	30–50	98.5	62.0	28.6 ± 10.4	69.3 ± 18.6	20.8 ± 9.0
S	30–50	99.6	77.1	34.1 ± 11.7	70.5 ± 17.4	24.4 ± 10.0
N	50–150	49.7	3.4	11.0 ± 6.6	8.0 ± 4.7	9.5 ± 6.2[b]
S	50–150	65.4	6.8	13.7 ± 7.3	7.8 ± 4.0	11.6 ± 6.8

[a]No energy dispersion applied; see full set in Table 3.

[b]Considered an upper limit.

when the energy dispersion is not applied, as previously reported in Table 3.

Table A2 shows that, with the exception of the soft (20–30 GeV) band, our approach is a conservative one, in that the inclusion of the energy dispersion actually enhances the detection. Even for the soft energy band, where these sources are brighter, however, the inclusion of the energy dispersion does not hamper significantly the detection of the source.

This paper has been typeset from a TEX/LATEX file prepared by the author.